

Mass-number and isotope dependence of local microscopic optical potential for polarized proton scattering

Masakazu Toyokawa,^{1,*} Kosho Minomo,^{1,†} and Masanobu Yahiro^{1,‡}

¹*Department of Physics, Kyushu University, Fukuoka 812-8581, Japan*

(Dated: March 5, 2018)

We derive local microscopic optical potentials U systematically for polarized proton scattering at 65 MeV using the local-potential version of the Melbourne g -matrix folding model. As target nuclei, we take ${}^6\text{He}$ and neutron-rich Ne isotopes in addition to stable nuclei of mass number $A = 4$ –208 in order to clarify mass-number and isotope dependence of U . The local potentials reproduce the experimental data systematically and have geometries similar to the phenomenological optical potentials for stable targets. The target density is broadened by the weak-binding nature and/or deformation of unstable nuclei. For the real spin-orbit part of U the density broadening weakens the strength and enlarges the radius, whereas for the central part it enlarges both of the strength and the radius. The density-broadening effect is conspicuous for halo nuclei such as ${}^6\text{He}$ and ${}^{31}\text{Ne}$. Similar discussions are made briefly for proton scattering at 200 MeV. We briefly investigate how the isovector and the non spherical components of U affect proton scattering.

PACS numbers: 25.40.Cm, 24.10.Ht, 24.70.+s

I. INTRODUCTION

Understanding of nucleon-nucleus (NA) and nucleus-nucleus (AA) interactions is one of the most important subjects in nuclear physics. The interactions (optical potentials) are necessary to describe not only elastic scattering but also more complicated reactions. Actually, the interactions are inputs of theoretical calculations, such as the distorted-wave Born approximation (DWBA) and the continuum discretized coupled-channels method (CDCC) [1–3], to analyze inelastic scattering and transfer and breakup reactions.

In general, NA elastic scattering is less absorptive and, hence, more sensitive to nuclear interior than AA scattering. Furthermore, one can determine not only the central part but also the spin-orbit part of the NA interaction, when the incident particle is polarized. Systematic measurements of polarized proton (p) elastic scattering have been made for stable target nuclei. As an outcome of the measurements, some global NA optical potentials have been constructed phenomenologically; see for example Refs. [4–7]. In most of the cases, the potentials are assumed to be local and thereby quite practical in many applications such as DWBA and CDCC calculations.

Elastic scattering of a polarized proton on unstable nuclei are a quite good tool used to investigate not only nuclear structures of unstable nuclei but also interactions between a proton and unstable nuclei, but the measurements are not easy. The first measurement on the vector analyzing power A_y was made by Uesaka and his collab-

orators for $p+{}^6\text{He}$ elastic scattering at 71 MeV with the inverse kinematics [8]. The g -matrix folding model yields reasonable agreement with the measured vector analyzing power [8]. The nuclear-medium effect included in the model is thus important for the observable. Recently, the effects of ${}^6\text{He}$ breakup on the elastic scattering were investigated with the eikonal approximation [9]. The medium effect is more significant than the breakup effect, as far as A_y is concerned.

The g -matrix folding model is a powerful tool to describe NA and AA interactions [10–19]. Particularly when the Melbourne g -matrix nucleon-nucleon (NN) interaction [17] is used, the model is successful in reproducing polarized proton elastic scattering from stable target nuclei systematically with no free parameter [17]. In the model, target-excitation and projectile-breakup effects are taken into account within the local-density approximation in addition to the medium effect. The microscopic optical potential derived by the model is non-local and thereby not so practical in many applications. It is, however, possible to localize the potential with the Brieva-Rook approximation [12]. Recently the validity of the approximation was shown in Ref. [20].

From a theoretical viewpoint based on the multiple scattering theory [21–23], a multiple NN scattering series in AA collisions [23] is more complicated than that in NA collisions [21, 22]. In this sense, microscopic understanding of AA interaction is relatively more difficult than that of NA interaction. Very recently, however, for AA elastic scattering the local microscopic optical potential was derived from the Melbourne g -matrix interaction by using both the folding model and the Brieva-Rook localization [24–26]. When the local-potential version of the Melbourne g -matrix folding model was applied to ${}^{12}\text{C}+{}^{12}\text{C}$ scattering at 6.2, 135, and 250 MeV/nucleon and ${}^{20-32}\text{Ne}+{}^{12}\text{C}$ scattering at 240 MeV/nucleon, the

*toyokawa@phys.kyushu-u.ac.jp

†minomo@phys.kyushu-u.ac.jp

‡yahiro@phys.kyushu-u.ac.jp

local potentials reproduced the measured elastic cross sections and reaction cross sections σ_R with no free parameter [24–26]. In the calculations, densities of unstable nuclei $^{20-32}\text{Ne}$ were evaluated by use of antisymmetrized molecular dynamics (AMD) [27, 28] with the Gogny-D1S interaction [29], whereas the phenomenological density [30] was taken for ^{12}C . The AMD wave functions successfully describe low-lying spectra of Ne isotopes [27]. The microscopic approach shows that $^{30-32}\text{Ne}$ in the “island of inversion” have large deformation and particularly ^{31}Ne is a deformed halo nucleus with spin-parity $3/2^-$ [24–26]. The local-potential version of the Melbourne g -matrix folding model is thus a powerful tool to determine structures of unstable nuclei. The success of the local-potential version of the Melbourne g -matrix folding model for proton scattering from stable nuclei and $^{20-32}\text{Ne}+^{12}\text{C}$ scattering implies that the model is reliable also for proton scattering from unstable nuclei such as Ne isotopes.

In this paper, we derive local microscopic optical potentials U systematically for polarized proton scattering at 65 MeV, using the local-potential version of the Melbourne g -matrix folding model. This local nature of U makes it easy to clarify global properties of U for both stable and unstable targets. As the targets, we consider ^6He and neutron-rich Ne isotopes in addition to stable nuclei of mass number $A = 4-208$. Throughout the global analyses, we clarify A and isotope dependence of U . Target densities are broadened much in ^6He and neutron-rich Ne isotopes compared with stable nuclei with the same A by the weak-binding nature and/or the nuclear deformation. We clarify how the density broadening affects the shape and the strength of U . This analysis is interesting particularly for ^6He and ^{31}Ne , since ^6He is a typical two-neutron halo nucleus and ^{31}Ne is a one-neutron halo nucleus with large deformation. Similar analyses are briefly made for proton scattering at 200 MeV. Finally, we briefly investigate how the isovector and the non-spherical components of U affect proton scattering.

We recapitulate the local-potential version of the Melbourne g -matrix folding model in Sec. II and show numerical results in Sec. III. Section IV is devoted to a summary.

II. THEORETICAL FRAMEWORK

Proton elastic scattering can be described by the one-body Schrödinger equation,

$$(T_R + U - E)\Psi^{(+)} = 0, \quad (1)$$

with a proton optical potential U , where E is an incident energy of proton and T_R is a kinetic-energy operator concerning the relative coordinate \mathbf{R} between an incident proton and a target. The optical potential U can be divided into the central (CE), the spin-orbit (LS), and the Coulomb (Coul) component as follows:

$$U = U_{\text{CE}} + U_{\text{LS}}\mathbf{L} \cdot \boldsymbol{\sigma} + V_{\text{Coul}}. \quad (2)$$

In the g -matrix folding model, U consists of the direct and exchange parts [31]. The exchange part is nonlocal, but it can be localized with the Brieva-Rook approximation [12]. Validity of the approximation is shown in Ref. [20]. We take this approximation in the present paper, since the localized U make it possible to make systematic analyses of U over stable and unstable targets. In addition to the merit, the local microscopic optical potential is quite useful in many applications, particularly when potentials between stable and unstable nuclei are needed in the applications.

The central part U_{CE} is then described by the sum of the direct component $U_{\text{CE}}^{\text{DR}}$ and the localized exchange component $U_{\text{CE}}^{\text{EX}}$ [12, 15, 18],

$$U_{\text{CE}} \equiv V_{\text{CE}} + iW_{\text{CE}} = U_{\text{CE}}^{\text{DR}} + U_{\text{CE}}^{\text{EX}} \quad (3)$$

with

$$U_{\text{CE}}^{\text{DR}}(\mathbf{R}) = \sum_{\alpha=p,n} \int \rho_{\alpha}(\mathbf{r}) g_{p\alpha}^{\text{DR}}(s; \rho_{\alpha}) d\mathbf{r}, \quad (4)$$

$$U_{\text{CE}}^{\text{EX}}(\mathbf{R}) = - \sum_{\alpha=p,n} \int \rho_{\alpha}(\mathbf{r}, \mathbf{r} - \mathbf{s}) g_{p\alpha}^{\text{EX}}(s; \rho_{\alpha}) j_0(K(R)s) d\mathbf{r}, \quad (5)$$

where V_{CE} (W_{CE}) is the real (imaginary) part of U_{CE} and $\mathbf{s} = \mathbf{r} - \mathbf{R}$, and \mathbf{r} is the coordinate of an interacting nucleon from the center-of-mass (c.m.) of target. The local momentum $\hbar K(R) \equiv \sqrt{2\mu_R(E - U_{\text{CE}} - V_{\text{Coul}})}$ present in Eq. (5) is obtained self-consistently, where μ_R is the reduced mass of the proton+target system.

Usually the direct part $g_{p\alpha}^{\text{DR}}$ and the exchange part $g_{p\alpha}^{\text{EX}}$ of the g -matrix interaction are assumed to be a function of the local density $\rho_{\alpha} = \rho_{\alpha}(\mathbf{r} - \mathbf{s}/2)$ at the midpoint of the interacting nucleon pair. The direct and exchange parts are described as

$$g_{pp}^{\text{DR,EX}}(s; \rho_p) = \frac{1}{4} (\pm g^{01} + 3g^{11}), \quad (6)$$

$$g_{pn}^{\text{DR,EX}}(s; \rho_n) = \frac{1}{8} (g^{00} \pm g^{01} \pm 3g^{10} + 3g^{11}), \quad (7)$$

in terms of the spin-isospin component g^{ST} of the g -matrix interaction.

Similar derivation is possible for the spin-orbit part U_{LS} [18],

$$U_{\text{LS}} \equiv V_{\text{LS}} + iW_{\text{LS}} = U_{\text{LS}}^{\text{DR}} + U_{\text{LS}}^{\text{EX}} \quad (8)$$

with

$$U_{\text{LS}}^{\text{DR}}(\mathbf{R}) = -\frac{1}{4R^2} \sum_{\alpha=p,n} \int \mathbf{R} \cdot \mathbf{s} \rho_{\alpha}(\mathbf{r}) g_{\text{LS},p\alpha}^{\text{DR}}(s; \rho_{\alpha}) d\mathbf{r}, \quad (9)$$

$$U_{\text{LS}}^{\text{EX}}(\mathbf{R}) = -\pi \sum_{\alpha=p,n} \int ds s^3 \left[\frac{2j_0(K(R)s)}{R} \rho_1^{(\alpha)}(R, s) + \frac{j_1(K(R)s)}{2k} \delta_0^{(\alpha)}(R, s) \right], \quad (10)$$

where V_{LS} (W_{LS}) is the real (imaginary) part of U_{LS} [see Appendix A for the definition of $\rho_1^{(\alpha)}(R, s)$ and

$\delta_0^{(\alpha)}(R, s)$]. As a g -matrix interaction, we take the Melbourne interaction [17] constructed from the Bonn-B nucleon-nucleon potential [32].

As target densities ρ , we consider three kinds of matter densities. For all the targets analyzed here, the matter densities are evaluated by spherical Hartree-Fock (HF) calculations with the Gogny-D1S interaction [29] in which the spurious center-of-mass motions are removed in the standard manner [26]. For lighter stable nuclei of $A \leq 40$, we also use the phenomenological proton-density [30] determined from electron scattering in which the finite-size effect of proton charge is unfolded in the usual way [33]. For each nucleus with $A \leq 40$, the neutron density is assumed to have the same geometry as the proton one, since the deviation of the neutron root-mean-square (rms) radius from the proton one is about 1% in the spherical HF calculation.

For $^{20-32}\text{Ne}$, the matter densities are evaluated also by AMD [27, 28] with the Gogny-D1S interaction [29]. This provides deformed matter densities. The AMD wave functions successfully describe low-lying spectra of Ne isotopes [27] and σ_R of $^{20-32}\text{Ne}+^{12}\text{C}$ scattering at 240 MeV/nucleon [24–26], and it is free from the spurious center-of-mass motion; see Ref. [26, 27] for the details of AMD calculations.

Particularly for ^{31}Ne with a quite small one-nucleon separation energy, we have to do a sophisticated calculation to make a tail correction to the AMD density, since the AMD density is inaccurate in its tail region. In principle, the ground state of ^{31}Ne can be described by the $^{30}\text{Ne}+n$ cluster model with core (^{30}Ne) excitations, and one can solve coupled equations for the model with the resonating group method (RGM) in which the ground and excited states of ^{30}Ne are constructed by AMD. This was done in Refs. [25, 26]. This method is referred to as AMD-RGM in this paper.

The matter density $\rho_{ImIm'}(\mathbf{r})$ is obtainable from the ground state wave function $\Phi_{\text{g.s.}}^{Im\pi}$ with spin I , its z -component m and parity π as

$$\rho_{ImIm'}(\mathbf{r}) = \langle \Phi_{\text{g.s.}}^{Im\pi} | \sum_i \delta(\mathbf{r}_i - \mathbf{X} - \mathbf{r}) | \Phi_{\text{g.s.}}^{Im'\pi} \rangle, \quad (11)$$

$$= \sum_{\lambda=0}^{2I} \rho_{II}^{(\lambda)}(r) (Im' \lambda \mu | Im) Y_{\lambda\mu}^*(\hat{r}), \quad (12)$$

where \mathbf{X} is the center-of-mass coordinate and \mathbf{r}_i is the coordinate of the i -th nucleon, and the summation over λ in Eq. (12) runs for even numbers. As the standard manner in the folding model, only the spherical ($\lambda = 0$) component of $\rho_{II}^{(\lambda)}$ is taken. This approximation makes the folding potential U spherical. This procedure is exact for even nuclei with $I = 0$, but approximate for odd nuclei with $I \neq 0$. The procedure is a good approximation for reaction cross sections of AA scattering at high incident energies [26]. We will examine in Sec. III E how accurate this procedure is for NA scattering.

III. RESULTS

In this section we analyze polarized proton scattering at $E = 65$ and 200 MeV, using the local-potential version of the Melbourne g -matrix folding model, although the analysis is mainly focused on the case of $E = 65$ MeV. In the folding model, we also consider the Franey-Love t -matrix NN interaction [34]. As target nuclei of proton scattering, we consider stable nuclei of ^4He , ^{12}C , ^{16}O , ^{20}Ne , ^{24}Mg , ^{40}Ca , ^{90}Zr , ^{208}Pb , and unstable nuclei of ^6He and neutron-rich Ne isotopes.

A. Proton scattering from stable nuclei at 65 and 200 MeV

In this subsection, we mainly consider proton scattering at 65 MeV and briefly discuss the case of 200 MeV at the end of this subsection.

Figure 1 shows elastic cross sections $d\sigma/d\Omega$ and vector analyzing powers A_y as a function of the scattering angle $\theta_{\text{c.m.}}$ for proton scattering at $E = 65$ MeV from ^4He , ^{12}C , ^{40}Ca , and ^{208}Pb targets. The solid lines denote the results of the local microscopic potentials derived from the Melbourne g -matrix interaction. The results are consistent with those [17] of the nonlocal microscopic potentials derived from the Melbourne g -matrix interaction, although target wave functions used in two calculations differ. The g -matrix folding model shown by the solid lines yields better agreement with the experimental data [35–42] than the t -matrix folding model denoted by the dashed lines. The medium effect shown by the difference between the solid and dashed lines are more significant for A_y . For lighter targets of ^4He , ^{12}C and ^{40}Ca , the agreement of the g -matrix folding model with the data is better for the phenomenological densities denoted by the solid lines than for the HF densities shown by the dotted lines. However, the g -matrix folding model with the HF density still keeps reasonable agreement with the data. The HF density based on the Gogny-D1S interaction [29] is thus quite useful to derive the microscopic optical potentials U systematically.

Figure 2 shows A dependence of the reaction cross sections σ_R for proton scattering. The closed circles (crosses) denote the results of the g -matrix (t -matrix) folding model with the phenomenological target densities for $A \leq 40$ and the HF target densities for $A > 40$. The g -matrix folding model yields better agreement with the data than the t -matrix folding model. The results of the g -matrix folding model agree with the data [43–47] within 10% error in a wide range of $4 \leq A \leq 208$. Since σ_R is sensitive to W_{CE} , the part is thus derived with at least 90% accuracy.

As a merit of deriving the local microscopic optical potential U , we can directly compare U with phenomenological optical potentials. Here we take two types of phenomenological optical potentials. One is the Koning-Delaroche (KD) optical potential [4] based on the stan-

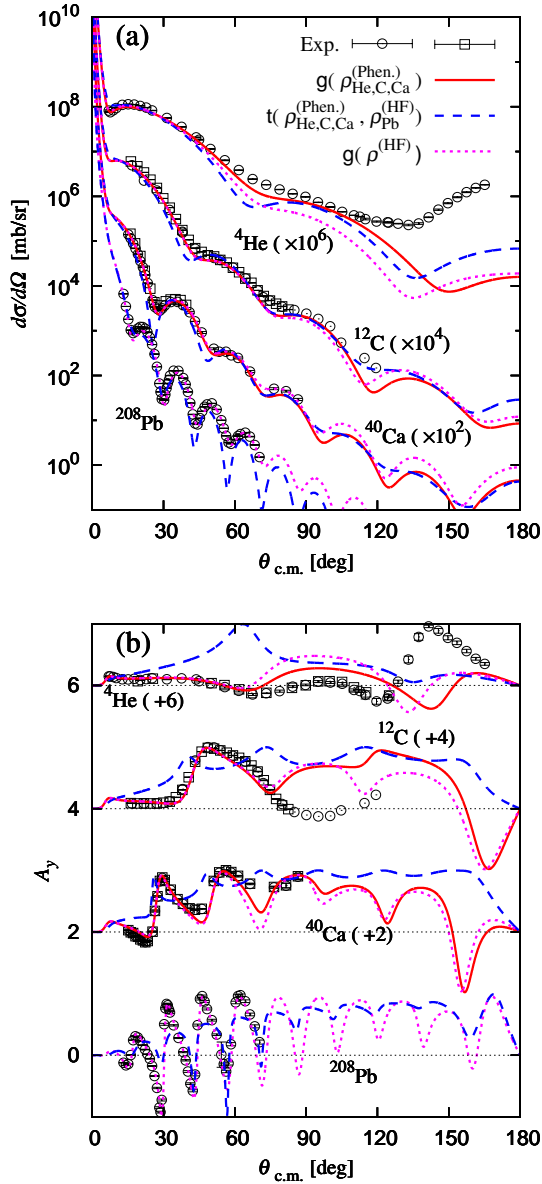


FIG. 1: (Color online) Angular distributions of (a) the elastic cross sections $d\sigma/d\Omega$ and (b) the vector analyzing powers A_y for proton scattering at $E = 65$ MeV from ${}^4\text{He}$, ${}^{12}\text{C}$, ${}^{40}\text{Ca}$, and ${}^{208}\text{Pb}$ targets. The solid (dotted) lines represent the results of the g -matrix folding model with the phenomenological (HF) density, whereas the dashed lines correspond to the results of the t -matrix folding model with the phenomenological density. Experimental data are taken from Refs. [35–42].

dard potential search in the framework of the Schrödinger equation, and another is the Dirac phenomenology optical potential [5, 6] based on the standard potential search in the framework of the Dirac equation. As an example, we compare the three optical potentials for $p+{}^{40}\text{Ca}$ scattering at $E = 65$ MeV in Fig. 3. The microscopic optical potential is calculated from the phenomenologi-

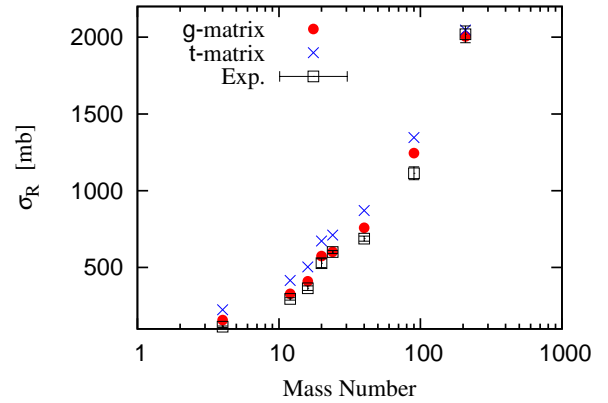


FIG. 2: (Color online) A dependence of the reaction cross sections σ_R for proton scattering at $E \approx 65$ MeV. The closed circles (crosses) stand for the results of the g -matrix (t -matrix) folding model with the phenomenological densities for $A \leq 40$ and the HF ones for $A > 40$. Experimental data are taken from Refs. [43–47], where $E = 47.9$ MeV for ${}^4\text{He}$, 65.5 MeV for ${}^{12}\text{C}$, ${}^{16}\text{O}$, ${}^{40}\text{Ca}$, and ${}^{208}\text{Pb}$; 47.0 MeV for ${}^{20}\text{Ne}$; 48.0 MeV for ${}^{24}\text{Mg}$; and 60.8 MeV for ${}^{90}\text{Zr}$.

cal target density. The imaginary spin-orbit part W_{LS} is about 10 times as small as V_{LS} , so it hardly affects the present elastic scattering. We then compare the three optical potentials for V_{CE} , W_{CE} and V_{LS} . The KD optical potential denoted by the dashed lines has R dependence similar to that of the Dirac phenomenology optical potential shown by the dotted lines. In the peripheral region, furthermore, R dependence of the two phenomenological optical potentials is similar to that of the microscopic one shown by the solid lines. At small R , the deviations of the microscopic optical potential from the phenomenological ones are small for V_{CE} , but become sizable for V_{LS} and W_{CE} . For V_{LS} the deviations little affect $d\sigma/d\Omega$ and A_y up to 90° where the experimental data is available, but for W_{CE} the deviations slightly enhance σ_R and consequently overestimate the measured σ_R by several percentages.

For the $p+{}^4\text{He}$ system, the g -matrix folding model does not reproduce the measured elastic cross sections at backward angles $\theta_{c.m.} \gtrsim 90^\circ$. A possible origin of this deviation is the heavy-ion (${}^3\text{H}$) exchange process that is not included in the folding model. The process generates a parity-dependent potential [48]. We then rewrite V_{CE} as

$$V_{CE} \rightarrow V_{CE}(1 + \alpha(-1)^L) \quad (13)$$

to incorporate the effect in the folding model phenomenologically. The parameter α is fitted to the experimental data [35, 36], and the resulting value is $\alpha = 0.13$. In Fig. 4, the solid (dashed) lines show $d\sigma/d\Omega$ and A_y calculated by the g -matrix folding model with $\alpha = 0.13$ ($\alpha = 0$). Effects of the parity-dependent potential are appreciable at intermediate angles $60^\circ \lesssim \theta_{c.m.} \lesssim 90^\circ$ and significant at backward angles at $\theta_{c.m.} \gtrsim 90^\circ$.

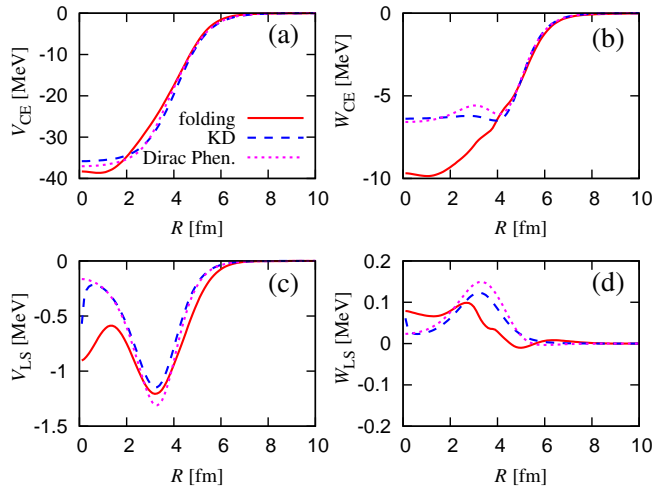


FIG. 3: (Color online) R dependence of the microscopic optical potential, the Koning-Delaroche (KD) optical potential and the Dirac phenomenology optical potential for $p+^{40}\text{Ca}$ scattering at $E = 65$ MeV. The microscopic optical potential is denoted by the solid lines, the Koning-Delaroche (KD) optical potential [4] by the dashed lines and the Dirac phenomenology optical potential by the dotted lines. Panels (a), (b), (c), and (d) correspond to V_{CE} , W_{CE} , V_{LS} , and W_{LS} , respectively.

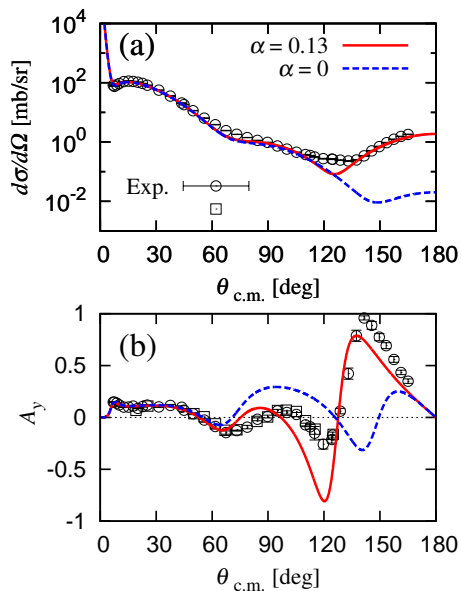


FIG. 4: (Color online) Effects of the parity-dependent potential on (a) the elastic cross section $d\sigma/d\Omega$ and (b) the vector analyzing power A_y for $p+^4\text{He}$ scattering at $E = 65$ MeV. The solid (dashed) lines stand for the results of the g -matrix folding model with $\alpha = 0.13$ ($\alpha = 0$), where the phenomenological density is taken for ^4He . Experimental data are taken from Refs. [35, 36].

For the $p+^{12}\text{C}$ system, the g -matrix folding model does not reproduce the measured A_y around $\theta_{\text{c.m.}} = 100^\circ$. Even the phenomenological optical potentials [4–6] cannot reproduce it. The parity-dependent potential does not solve this problem, since the potential enhances the elastic cross section largely at $\theta_{\text{c.m.}} > 90^\circ$. Therefore this is an open problem. Except for the measured A_y around $\theta_{\text{c.m.}} = 100^\circ$ for the $p+^{12}\text{C}$ system, the g -matrix folding model yields good agreement with the data for targets of $A = 4\text{--}208$.

Now we briefly analyze proton scattering at $E = 200$ MeV as an example of intermediate energies and a typical case of beam energies in Radioactive Isotope Beam Factory (RIBF).

Figure 5 shows angular distributions of $d\sigma/d\Omega$ and A_y for proton scattering from stable nuclei ^4He , ^{12}C , ^{40}Ca , and ^{208}Pb . The definition of lines is the same as in Fig. 1. The g -matrix folding model with the phenomenological density, shown by the solid lines, reproduces the data [51–54] particularly at forward angles $\theta_{\text{c.m.}} \lesssim 60^\circ$. If Fig. 5 is compared with Fig. 1 as a function of the transferred momentum, $\theta_{\text{c.m.}} = 60^\circ$ in Fig. 5 corresponds to $\theta_{\text{c.m.}} = 128^\circ$ in Fig. 1. Therefore, the angle region $\theta_{\text{c.m.}} > 60^\circ$ in Fig. 5 corresponds to very backward angles $\theta_{\text{c.m.}} > 128^\circ$ in Fig. 1. In this sense, it is natural that in Fig. 5 the solid lines are deviated from the data at $\theta_{\text{c.m.}} \gtrsim 60^\circ$ particularly for lighter targets of $A \leq 12$. Even at $\theta_{\text{c.m.}} \gtrsim 60^\circ$ for lighter targets of $A \leq 12$, the g -matrix folding model with the phenomenological density, shown by the solid lines, yields better agreement with the data than that with the HF density denoted by the dotted lines. The medium effect, shown by the difference between the solid and dashed lines, is still significant at $E = 200$ MeV.

B. $p+^6\text{He}$ scattering at 71 and 200 MeV

As a typical example of proton scattering from unstable targets, we first consider $p+^6\text{He}$ scattering at 71 MeV, since the experimental data are available not only for $d\sigma/d\Omega$ but also for A_y . The ^6He density is obtained by the $^4\text{He}+n+n$ orthogonality-condition model; see Refs. [49, 50] for the details. As a ^4He density in the model, we take either the phenomenological or the HF density. In Fig. 6, the solid (dashed) lines show $d\sigma/d\Omega$ and A_y calculated by the g -matrix (t -matrix) folding model with the phenomenological ^4He density, whereas the dotted lines correspond to the results of the g -matrix folding model with the HF ^4He density. The g -matrix folding model shown by the solid lines yields better agreement with the data [8, 55] than the t -matrix folding model denoted by the dashed lines. The solid lines are consistent with the results of the nonlocal microscopic optical potential derived from the Melbourne g -matrix interaction [8], although ^6He wave functions used in two calculations differ.

In Fig. 6, the differences between the solid and dotted lines come from the difference between the phenomenological and HF ^4He densities. Comparing Fig. 6 with

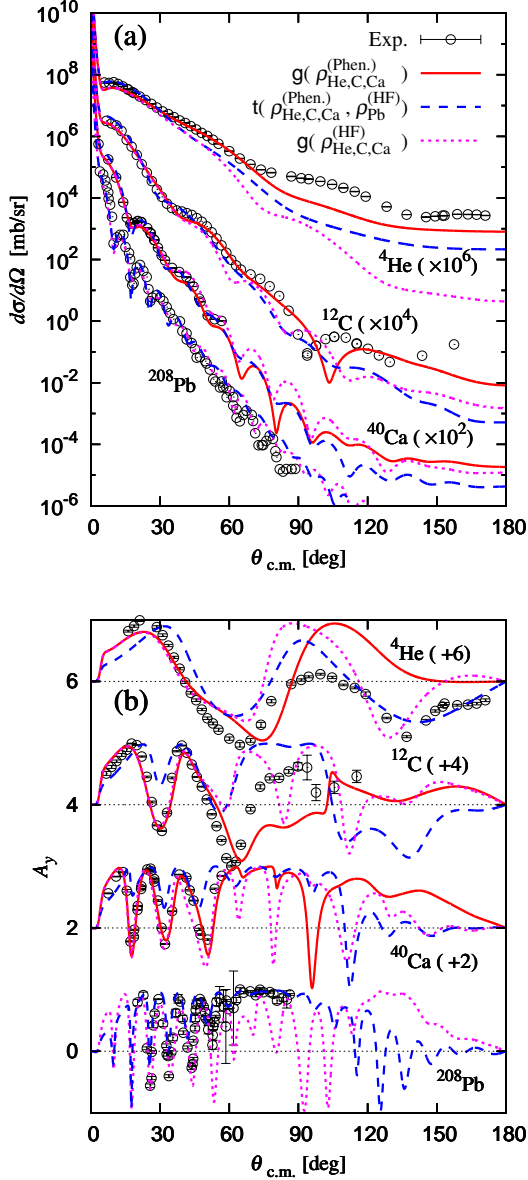


FIG. 5: (Color online) Angular distributions of (a) the elastic cross sections $d\sigma/d\Omega$ and (b) the vector analyzing powers A_y for proton scattering at $E = 200$ MeV from ${}^4\text{He}$, ${}^{12}\text{C}$, ${}^{40}\text{Ca}$, and ${}^{208}\text{Pb}$ targets. See Fig. 1 for the definition of lines. Experimental data are taken from Refs. [51–54].

Fig. 1, one can see that the difference in the ${}^4\text{He}$ density yields smaller effects on $d\sigma/d\Omega$ and A_y in $p+{}^6\text{He}$ scattering than in $p+{}^4\text{He}$ scattering. The difference in the ${}^4\text{He}$ density is thus partly masked by densities of extra two neutrons in the $p+{}^6\text{He}$ scattering.

In Fig. 6, the nuclear-medium effect is shown by the differences between the solid and dashed lines, and the effect is much more significant for A_y than $d\sigma/d\Omega$. The differences mainly come from the fact that W_{CE} calculated with the g -matrix folding model is much less ab-

sorptive than that with the t -matrix folding model; see Fig. 7 for R dependence of U .

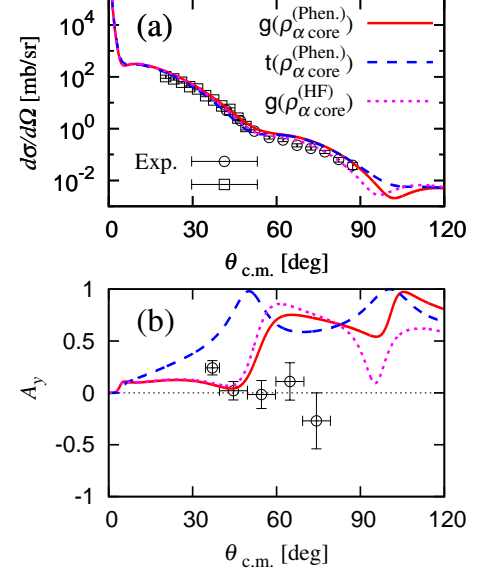


FIG. 6: (Color online) Angular distributions of (a) the elastic cross section $d\sigma/d\Omega$ and (b) the vector analyzing power A_y for $p+{}^6\text{He}$ scattering at $E = 71$ MeV calculated by the folding model with the ${}^4\text{He}+n+n$ model density. The solid (dotted) lines represent the results of the g -matrix folding model with the phenomenological (HF) ${}^4\text{He}$ density, whereas the dashed lines correspond to the results of the t -matrix folding model with the phenomenological ${}^4\text{He}$ density. Experimental data are taken from Ref. [8, 55].

As mentioned above, the g -matrix folding model yields better agreement with the data than the t -matrix folding model. The agreement is, however, not perfect particularly for A_y . The parity-dependent potential little works at forward angles $\theta < 90^\circ$ in which the experimental data are available. We then make a potential search to see what causes the difference between the theoretical and experimental results. Here we change the strength of U as

$$U \rightarrow (f_V^{\text{CE}}V_{\text{CE}} + if_W^{\text{CE}}W_{\text{CE}}) + (f_V^{\text{LS}}V_{\text{LS}} + if_W^{\text{LS}}W_{\text{LS}})\mathbf{L} \cdot \boldsymbol{\sigma} + V_{\text{Coul}} \quad (14)$$

with adjustable parameters f_V^{CE} , f_W^{CE} , f_V^{LS} , f_W^{LS} . A best fit is obtained at $(f_V^{\text{CE}}, f_W^{\text{CE}}, f_V^{\text{LS}}, f_W^{\text{LS}}) = (0.7, 0.7, 0.9, 4.0)$, but $d\sigma/d\Omega$ and A_y are not so sensitive at $\theta > 40^\circ$ to variations of f_W^{CE} and f_V^{LS} and hence these parameters are not determined sharply.

Figure 8 shows the potential search for $p+{}^6\text{He}$ scattering at $E = 71$ MeV. The solid lines represent the results of the potential search, whereas the dashed lines mean the results of the g -matrix folding model with the phenomenological ${}^4\text{He}$ density. A small reduction of $d\sigma/d\Omega$ from the dashed to the solid line at $\theta > 50^\circ$ mainly comes

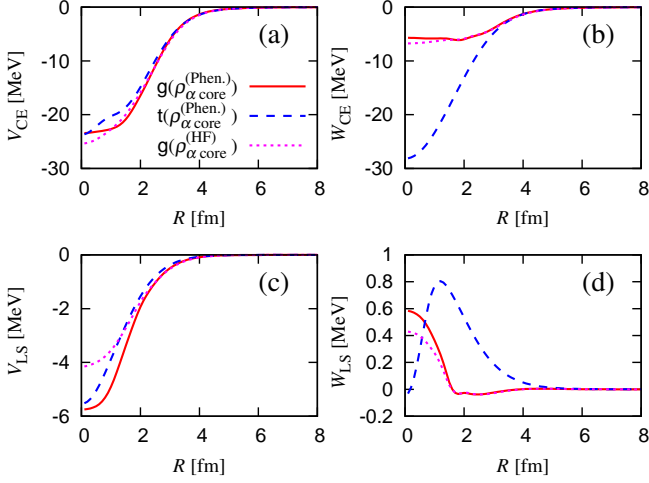


FIG. 7: (Color online) R dependence of the microscopic optical potential for $p+{}^6\text{He}$ scattering at $E = 71$ MeV. See Fig. 6 for the definition of lines. Panels (a), (b), (c), and (d) correspond to V_{CE} , W_{CE} , V_{LS} , and W_{LS} , respectively.

from the reduction of V_{CE} , and a large change of A_y from the dashed to the solid line at $\theta > 40^\circ$ is mainly originated in the increase of W_{LS} . Thus the large enhancement of W_{LS} is necessary, but it is not clear what causes the large enhancement of W_{LS} . This is an interesting question to be solved in the future.

Now we briefly analyze proton scattering from ${}^6\text{He}$ at $E = 200$ MeV. Any experimental data is not available for this energy at the present stage, but the measurements particularly of A_y are planned in RIBF. Figure 9 shows angular distributions of $d\sigma/d\Omega$ and A_y for proton scattering from ${}^6\text{He}$ at $E = 200$ MeV. The definition of line is the same as in Fig. 6. As shown in Fig. 5, the g -matrix folding model shown by the solid lines yields consistent results with the data for stable target nuclei. Hence, the model prediction, shown by the solid lines in Fig. 9, is expected to be reliable also for ${}^6\text{He}$, particularly at forward angles $\theta_{\text{c.m.}} \lesssim 60^\circ$. At backward angles $\theta_{\text{c.m.}} \gtrsim 60^\circ$, the solid lines differ from the dashed and dotted lines. This means that it is necessary to include the medium effect and use the phenomenological ${}^4\text{He}$ density there.

C. A dependence of microscopic optical potentials

The g -matrix folding model is successful in reproducing the data on polarized proton scattering for targets of $A = 12$ –208. In general, the g -matrix folding model is considered to be less accurate for light targets such as ${}^4, {}^6\text{He}$, since the g -matrix interaction is evaluated in nuclear matter and the local density approximation used seems to be more reliable for heavier targets. Nevertheless, the agreement of the model calculations with the data is still reasonable for light targets ${}^4, {}^6\text{He}$. We then

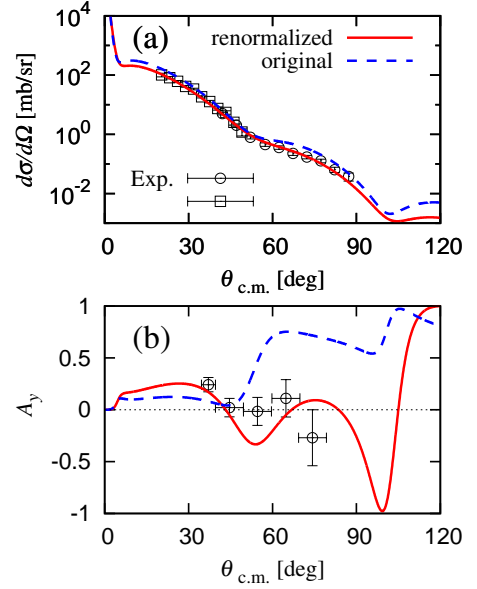


FIG. 8: (Color online) Potential search for $p+{}^6\text{He}$ scattering at $E = 71$ MeV in (a) the elastic cross sections $d\sigma/d\Omega$ and (b) the vector analyzing powers A_y . The solid lines represent the best-fit result with $(f_V^{\text{CE}}, f_W^{\text{CE}}, f_V^{\text{LS}}, f_W^{\text{LS}}) = (0.7, 0.7, 0.9, 4.0)$, whereas the dashed lines correspond to the original results. Experimental data are taken from Refs. [8, 55].

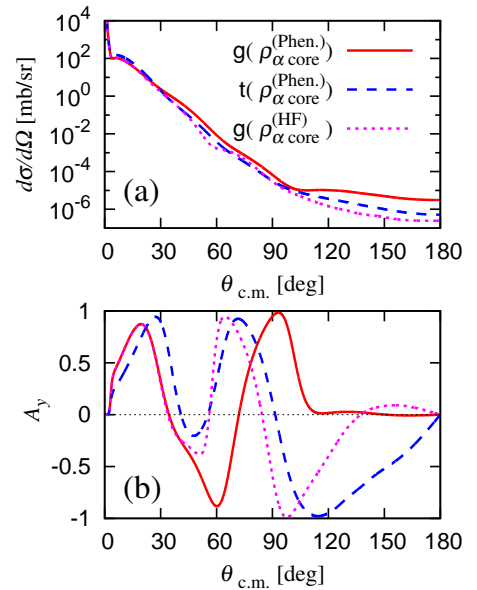


FIG. 9: (Color online) Angular distributions of (a) the elastic cross section $d\sigma/d\Omega$ and (b) the vector analyzing power A_y for proton scattering from ${}^6\text{He}$ at $E = 200$ MeV. See Fig. 6 for the definition of lines.

	a_1	a_2	a_3	a_4
V_{CE}	-0.0023	0.0104	0.8508	1.0578
W_{CE}	-0.0076	0.0473	0.8732	1.332
V_{LS}	-0.0033	0.0137	1.2305	-0.0682

TABLE I: Parameter fitting for A dependence of the rms radius of U with a functional form $a_1A + a_2A^{2/3} + a_3A^{1/3} + a_4$. All the parameters are presented in units of fm.

derive global properties of the local microscopic optical potentials for proton scattering at 65 MeV. The potentials are calculated with the g matrix folding model with the phenomenological target densities for $A \leq 40$ and the HF densities for $A > 40$.

Since the microscopic optical potentials do not have any simple shape, we consider the volume integral J and the rms radius $\langle R^2 \rangle^{1/2}$ for each part of U :

$$J = \int F(R)d\mathbf{R}, \quad \langle R^2 \rangle^{1/2} = \sqrt{\int R^2 F(R)d\mathbf{R}/J}, \quad (15)$$

where $F(R)$ represents each part of U . As shown in Figs. 3 and 7, W_{LS} is much smaller than V_{LS} and hence yields no significant effect on the present systems. Furthermore, meanings of the volume integral and the rms radius are not clear for W_{LS} , since W_{LS} is an oscillating function of R . For these reasons, we do not consider the volume integral and the rms radius of W_{LS} here.

Figure 10 shows the rms radius of U as a function of A . For each part of U , A dependence of the rms radius is determined for stable targets of $A = 4$ –208 by a curve

$$a_1A + a_2A^{2/3} + a_3A^{1/3} + a_4; \quad (16)$$

see Table I for the results of the fitting. The fitting line is referred to as the stable-nucleus line. For each panel, the lower figure shows a ratio of the rms radius to the stable-nucleus line. Since ${}^6\text{He}$ has a halo structure, the ${}^6\text{He}$ rms radius is enlarged by the structure from the stable-nucleus line by $\sim 18\%$ for V_{CE} , $\sim 25\%$ for W_{CE} and $\sim 12\%$ for V_{LS} . The large enhancement of ${}^6\text{He}$ rms radius in W_{CE} means that the reaction cross section is a good tool of searching for halo nuclei and determining their radii.

We consider the reason why the enhancement of ${}^6\text{He}$ rms radius is larger in V_{CE} than in V_{LS} . For this purpose, we show A dependence of rms radii of ρ and $d\rho/dr$ in Fig. 11. In the short-range limit of the g -matrix interaction, the shape of V_{CE} (V_{LS}) is approximately determined by that of ρ ($d\rho/dr$). The enhancement of ${}^6\text{He}$ rms radius from the stable-nucleus line is smaller for $d\rho/dr$ than for ρ , as shown in Fig. 11; see Table II for the stable-nucleus (dotted) line.

Figure 12 shows the volume integral of U as a function of A , and the parameters of the fits for the stable nuclei are shown in Table III. The volume integral is also enhanced at $A = 6$ from the stable nucleus line by the halo

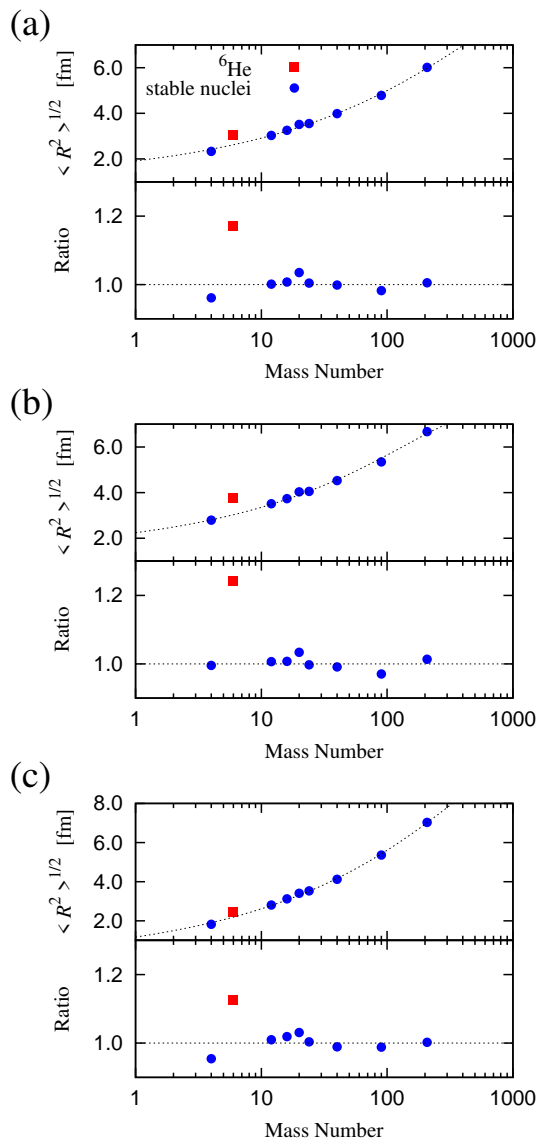


FIG. 10: (Color online) A dependence of the rms radius of the microscopic optical potential at 65 MeV. The A dependence is shown by the circles for stable targets and by the squares for ${}^6\text{He}$ target. Panels (a), (b), and (c) correspond to V_{CE} , W_{CE} , and V_{LS} , respectively. See Table I for the parameter set of the stable-nucleus (dotted) line.

	a_1	a_2	a_3	a_4
ρ	-0.0074	0.0378	0.9578	-0.0022
$d\rho/dr$	-0.0079	0.0402	1.2478	-0.2322

TABLE II: Parameter fitting for A dependence of rms radii of ρ and $d\rho/dr$ with a functional form $a_1A + a_2A^{2/3} + a_3A^{1/3} + a_4$. All the parameters are presented in units of fm.

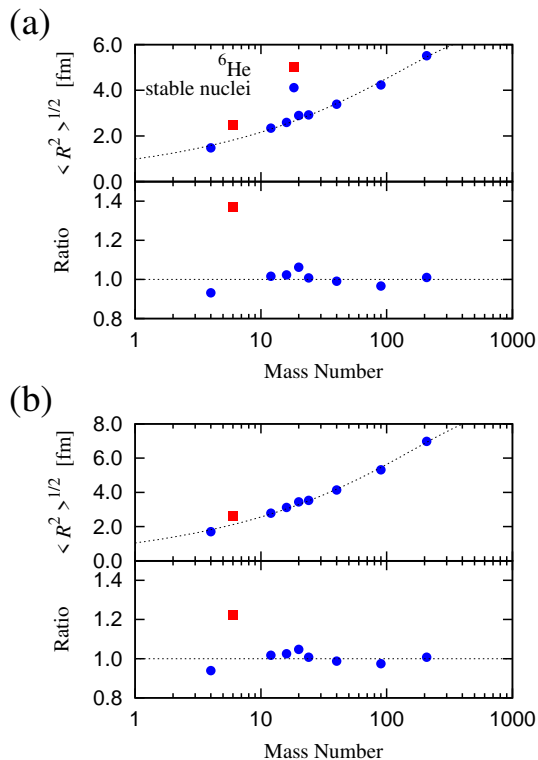


FIG. 11: (Color online) A dependence of rms radii of (a) ρ and (b) $d\rho/dr$. See Fig. 10 for the definition of symbols and Table II for the parameter set of the stable-nucleus (dotted) line.

	a_1	a_2	a_3	a_4
V_{CE}	301.28	-59.695	272.22	-125.78
W_{CE}	81.082	92.201	301.22	-439.22
V_{LS}	0.093	6.24	95.645	105.11

TABLE III: Parameter fitting for A dependence of the volume integral of U with a functional form $a_1 A + a_2 A^{2/3} + a_3 A^{1/3} + a_4$. All the parameters are presented in units of MeV fm^3 .

structure of ${}^6\text{He}$. This enhancement is larger in W_{CE} than in V_{CE} . In V_{LS} , meanwhile, the volume integral is suppressed at $A = 6$ from the stable nucleus line. The halo structure of ${}^6\text{He}$ makes ρ broader and, hence, suppresses $d\rho/dr$ and, consequently, weakens the strength of V_{LS} .

Finally, we show A dependence of σ_R in Fig. 13 for proton scattering at $E = 65$ MeV. The reaction cross section is enhanced for ${}^6\text{He}$ by $\sim 35\%$ from the stable-nucleus (dotted) line; see Table IV for the parameter set. This enhancement is a result of the corresponding enhancement of W_{CE} in its rms radius and volume integral.

Throughout all the analyses in this subsection, one can find that the broadening of ${}^6\text{He}$ density due to halo structure (weak-binding nature) yields significant effects on U . The effect differs between the central and spin-orbit parts

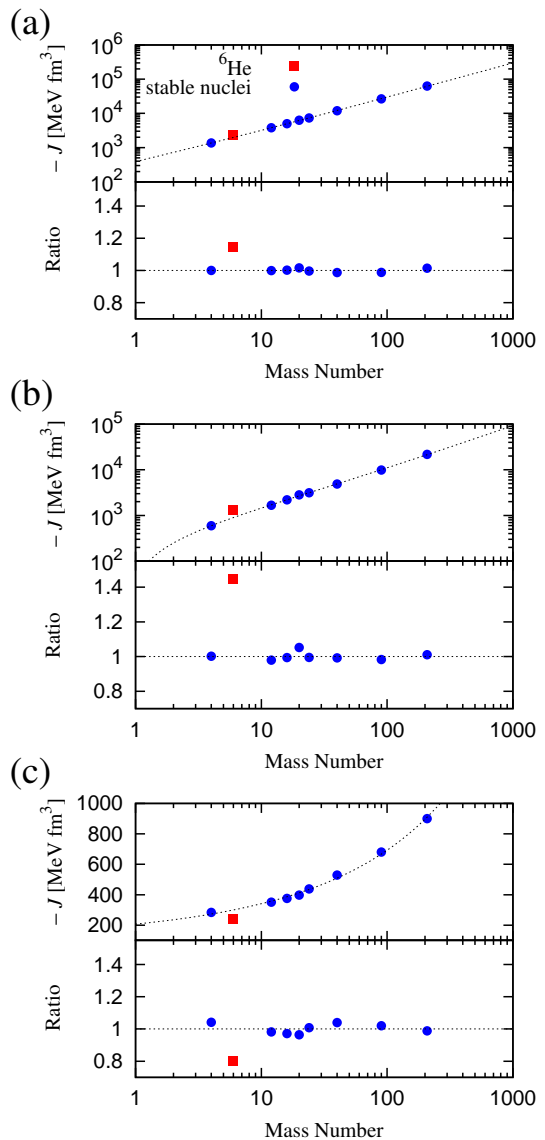


FIG. 12: (Color online) A dependence of the volume integral of the microscopic optical potential at 65 MeV. Panels (a), (b), and (c) correspond to V_{CE} , W_{CE} , and V_{LS} , respectively. See Fig. 10 for the definition of symbols and Table III for the parameter set of the stable-nucleus (dotted) line.

of U . For the central part, it enhances the strength and the rms radius by about $20\% \sim 40\%$. For V_{LS} , meanwhile, the broadening enlarges the rms radius by about 10% but weakens the strength by about 20% .

D. Isotope dependence of microscopic optical potential

The broadening of matter densities is induced by the weak-binding nature for unstable nuclei and by the deformation for largely deformed nuclei. Deformation is a

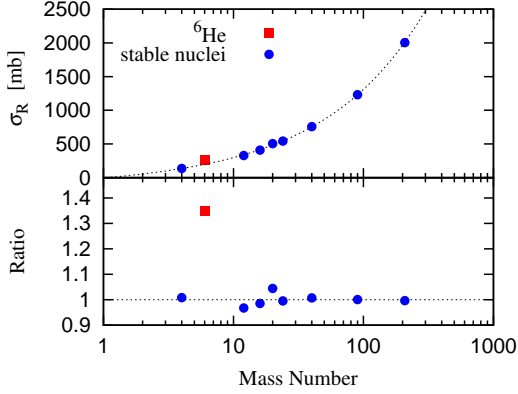


FIG. 13: (Color online) A dependence of the reaction cross sections for proton scattering at $E = 65$ MeV. See Fig. 10 for the definition of symbols and Table IV for the parameter set of the stable-nucleus (dotted) line.

	a_1	a_2	a_3	a_4
σ_R	-0.6797	45.534	122.34	-170.78

TABLE IV: Parameter fitting for A dependence of σ_R with a functional form $a_1 A + a_2 A^{2/3} + a_3 A^{1/3} + a_4$. All the parameters are presented in units of mb.

picture in the body-fixed frame. Hence, the deformed density in the body-fixed frame should be transformed into the corresponding ground-state density in the space-fixed frame by making the angular-momentum projection. This was done properly in Eq. (12). The projection makes the spherical ($\lambda = 0$) part of the ground-state density broad.

The local-potential version of the Melbourne g -matrix folding model is successful in reproducing both $^{20-32}\text{Ne} + ^{12}\text{C}$ scattering and proton scattering from stable nuclei at 65 MeV. This indicates that the model is reliable also for proton scattering from $^{20-32}\text{Ne}$ at 65 MeV. Now we analyze the proton scattering with the local-potential version of the folding model in order to investigate how large weak-binding and deformation effects are on U and σ_R . The analysis is particularly interesting for ^{31}Ne , since it is a one-neutron halo nucleus with large deformation.

Figure 14 shows isotope dependence of σ_R for $p + ^{20-32}\text{Ne}$ scattering at 65 MeV. The dotted line denotes the stable-nuclei line for σ_R ; see Table IV for the results of the fitting. The triangles represent the results of the g -matrix folding model with the spherical HF densities, whereas the closed circles correspond to those with the AMD densities in which Ne isotopes are deformed. The deviation of the triangles from the dotted line represents the weak-binding effect, whereas that of the closed circles from the triangles shows the deformation effect. Here, the weak-binding effect includes the effects of neutron

skin. These effects are more apparent in the lower panel where the σ_R for ^ANe are normalized by those for stable nuclei with the same A . At $20 \leq A \leq 23$, the deformation effect is more significant than the weak-binding effect. Since the weak-binding effect becomes large as A increases, the effect is more important than the deformation effect at $24 \leq A \leq 30$. For $A = 31, 32$, Ne isotopes have no bound state in the spherical HF calculation. In this sense, both the deformation and the weak-binding effect are important there.

For ^{31}Ne , the one-neutron separation energy is quite small. We then do a AMD-RGM calculation to make a tail correction to the AMD density. The closed square denotes the result of the AMD-RGM density, and the deviation of the closed square from the stable-nucleus line represents a net effect of halo structure and deformation. This effect is detectable from the measurements of σ_R or the one-neutron removal cross section. Actually, this was done for the $^{31}\text{Ne} + ^{12}\text{C}$ system at 240 MeV/nucleon [24–26, 56, 57].

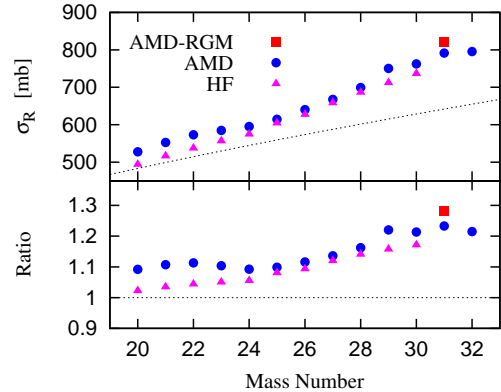


FIG. 14: (Color online) Isotope dependence of the reaction cross sections for $p + ^{20-32}\text{Ne}$ scattering at 65 MeV. The circles (triangles) show the results of the AMD (HF) densities, and the square for ^{31}Ne is the result of the AMD-RGM density. See Table IV for the parameter set of the stable-nucleus (dotted) line.

Figures 15 and 16 show the volume integral and the rms radius of U for $p + ^{20-32}\text{Ne}$ scattering at 65 MeV, respectively. The weak-binding and nuclear-deformation effects play the same role between U and σ_R . Actually, the deformation effect is more important than the weak-binding effect at $20 \leq A \leq 23$, whereas the latter is more significant than the former at $24 \leq A \leq 30$. The density-broadening effect due to weak-binding nature and deformation in Ne isotopes is the same as that due to weak-binding nature in ^6He . For ^{31}Ne as a typical case, it suppresses the volume integral by about 10% and enlarges the rms radius by about 5% for V_{LS} , whereas it enlarges both the volume integral and the rms radius by about 10% for V_{CE} and W_{CE} . The imaginary central part W_{CE} is more sensitive to the density-broadening ef-

fect than the other parts. Thus σ_R is a good quantity to investigate the density broadening.

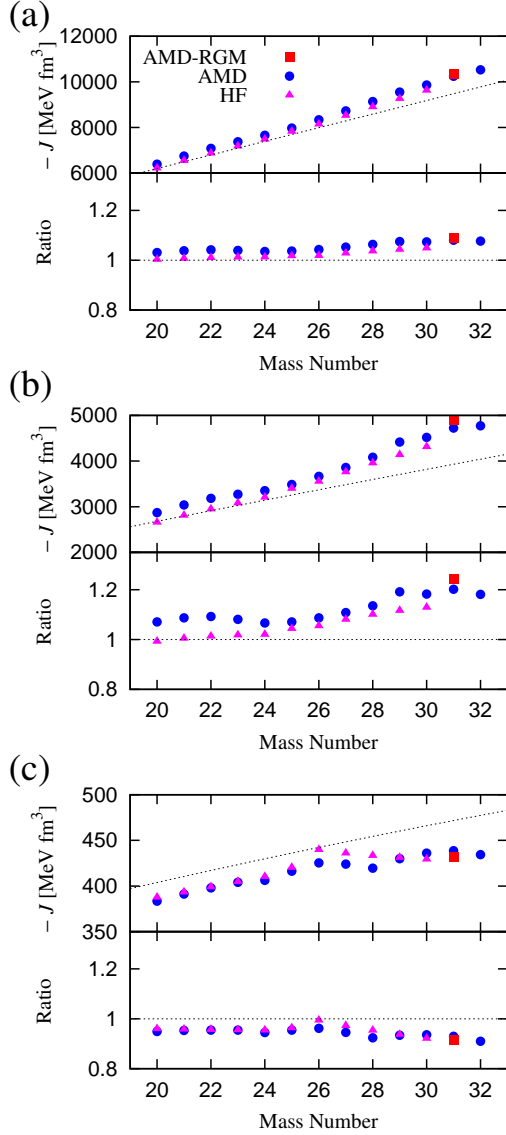


FIG. 15: (Color online) A dependence of the volume integral of the microscopic optical potential for $p+^{20-32}\text{Ne}$ scattering at 65 MeV. Panels (a), (b) and (c) correspond to V_{CE} , W_{CE} and V_{LS} , respectively. See Fig. 14 for the definition of symbols and Table III for the parameter set of the stable-nucleus (dotted) line.

E. Nuclear deformation effects on elastic scattering

If a target nucleus is strongly deformed, the deformation affects proton elastic scattering. For example, $^{22,30}\text{Ne}$ and their neighborhood nuclei are known to be well deformed. For even target nuclei with $I = 0$, nuclear deformation yields two kinds of effects. First, it enlarges

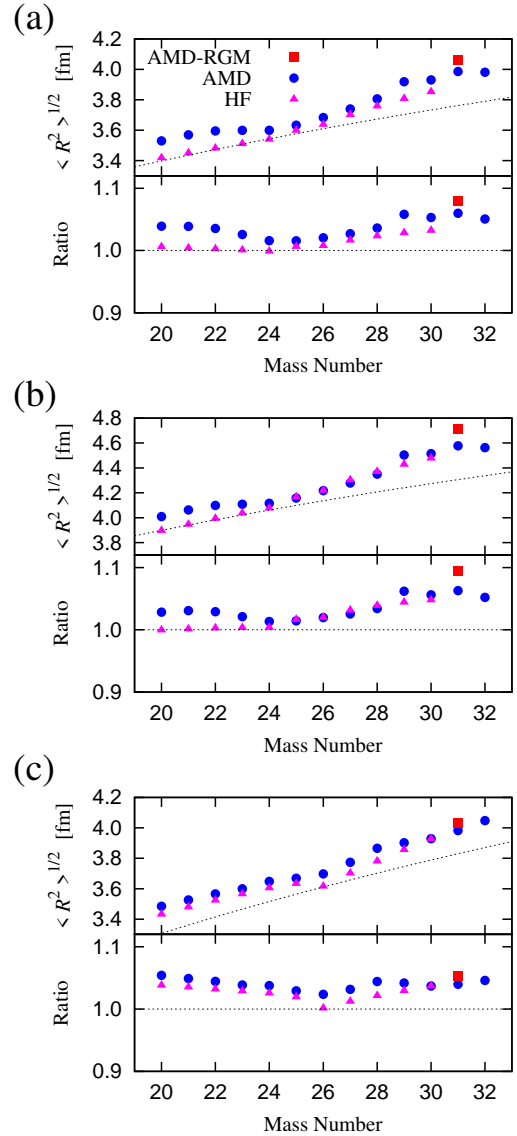


FIG. 16: (Color online) A dependence of the rms radius of the microscopic optical potential for $p+^{20-32}\text{Ne}$ scattering at 65 MeV. Panels (a), (b) and (c) correspond to V_{CE} , W_{CE} and V_{LS} , respectively. See Fig. 14 for the definition of symbols and Table I for the parameter set of the stable-nucleus (dotted) line.

the spherical part of the target density and then the spherical part of U , as mentioned in Sec. III D. Second, the deformation enhances target excitations and then the back reactions to the elastic channel. The target-excitation effects are investigated in this subsection.

We consider proton elastic scattering from $^{22,30}\text{Ne}$, and rotational excitations to the 2^+ excited states are treated with the coupled-channel method. Transition densities between the elastic and inelastic channels are constructed by the deformed Woods-Saxon (DWS) model [26] with the quadrupole deformation parameter (β_2) evaluated by AMD; here the other parameters of the DWS model are

already determined to reproduce spectroscopic properties of high-spin states from light to heavy deformed nuclei, e.g., the quadrupole moments, the moments of inertia and the rms radii. Coupling potentials between the elastic and inelastic channels are obtained by folding the Melbourne g -matrix interaction with the transition densities.

Figure 17 shows angular distributions for $p+^{22}\text{Ne}$ scattering at 35 MeV. In this case, AMD yields $\beta_2 = 0.4$ [26]. The solid lines denote the results of the coupled-channel calculations, while the dotted and dot-dashed lines correspond to the results of the single-channel calculations with and without deformation, respectively. The solid line reproduces the experimental data [58] on both the elastic and the inelastic scattering with no adjustable parameter. The deviation of the solid line from the dotted line shows target-excitation effects, while the deviation of the dotted line from the dot-dashed one corresponds to density-broadening effects due to deformation. These effects are small at forward angles $\theta_{c.m.} \lesssim 60^\circ$, but become appreciable at middle and backward angles $\theta_{c.m.} \gtrsim 60^\circ$, although the target-excitation effects are relatively larger than the density-broadening effects. As for σ_R , the target-excitation effects are 4 %, whereas the density-broadening effects are about 5 %. The two effects are thus comparable for σ_R at this lower incident energy.

Similar analyses are made in Fig. 18 for $p+^{30}\text{Ne}$ scattering at 65 MeV; here AMD yields $\beta_2 = 0.4$ [26]. Target-excitation and density-broadening effects become appreciable at intermediate and backward angles $\theta_{c.m.} \gtrsim 50^\circ$, the two effects are comparable there. As for σ_R , the target-excitation effects are 2 %, while the density-broadening effects are about 4 %. At relatively higher incident energies such as 65 MeV, target-excitation effects are thus as small as density-broadening effects due to deformation, whereas density-broadening effects due to weak binding are about 20 % as shown in Fig. 14. Density-broadening effects due to weak binding thus become most significant for unstable target nuclei.

For odd target nuclei with $I > 0$, nuclear deformation induces another effect in addition to density-broadening and target-excitation effects. Namely the deformation makes the folding potential U non spherical, as seen in Eq. (12), and consequently induces a reorientation of target spin in proton scattering. We briefly investigate the reorientation effects here.

For targets with $I = 1/2^\pm$, we numerically confirmed that the reorientation effects are quite small on both reaction cross sections and differential elastic cross sections. Then we consider the case of $I = 3/2^-$ here. Figure 19 shows differential cross sections for proton elastic scattering from a $^{31}\text{Ne}(3/2^-)$ target at 65 MeV. Here the deformed target density, which is calculated by the DWS model with $\beta_2 = 0.42$ evaluated by AMD, is transformed into the corresponding ground-state density by the angular momentum projection. For simplicity, we neglect the spin-orbit interaction. The solid and dotted lines are the results of the folding-model calculations with and without reorientation effects, respectively. The effects are

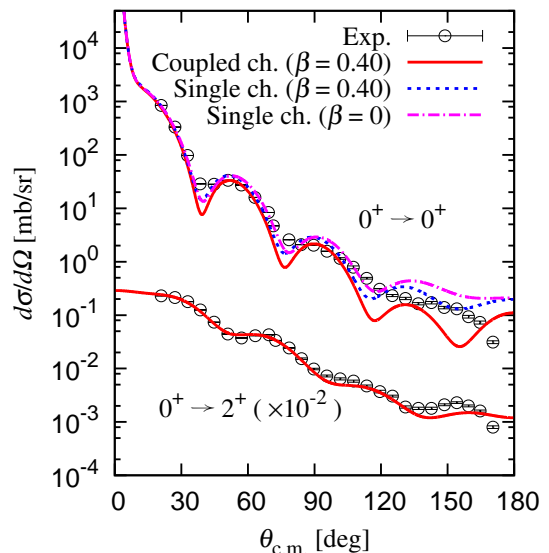


FIG. 17: (Color online) Angular distributions of the differential cross sections for proton elastic and inelastic scattering from ^{22}Ne at 35 MeV. The solid lines are the results of the coupled-channel calculations, while the dotted and dot-dashed lines correspond to the results of the single-channel calculations with and without deformation. The experimental data are taken from Ref. [58].

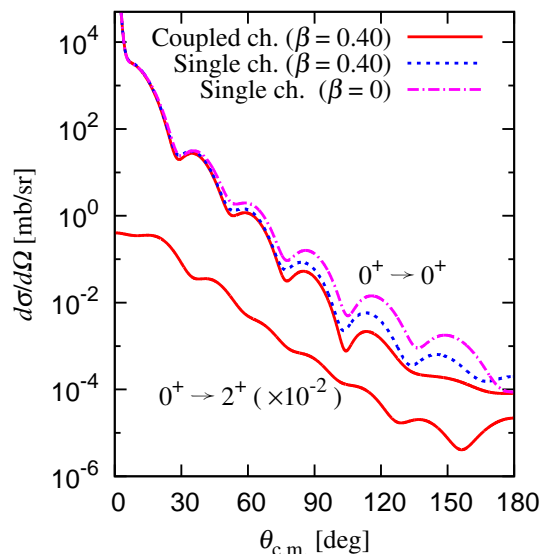


FIG. 18: (Color online) Angular distributions of the differential cross sections for proton elastic and inelastic scattering from ^{30}Ne at 65 MeV. See Fig. 17 for the definition of lines.

quite small at forward angles $\theta_{c.m.} \lesssim 50^\circ$ and become significant at middle and backward angles $\theta_{c.m.} \gtrsim 50^\circ$. Meanwhile, the effects are less than 1% on reaction cross sections. Reorientation effects are thus important for differential cross sections at middle and backward angles, but quite small for reaction cross sections.

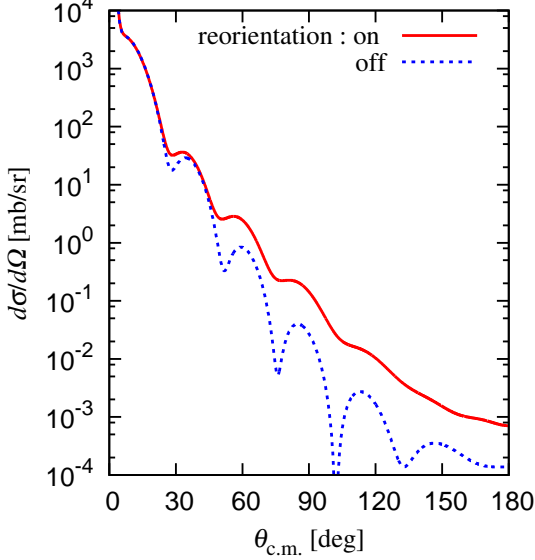


FIG. 19: (Color online) Angular distribution of the elastic cross section $d\sigma/d\Omega$ for $p+^{31}\text{Ne}$ elastic scattering at 65 MeV. The solid (dotted) line shows the result of the folding-model calculation with (without) reorientation effects.

F. Isovector components of optical potentials

In this subsection, we discuss effects of the isovector component of U briefly. For simplicity, we neglect the spin-orbit part of U , since the effect is negligible for the $p+^{20-32}\text{Ne}$ systems at 65 MeV analyzed here. In general, the central part of nucleon optical potentials can be decomposed into the isoscalar and isovector components, U_0 and U_1 , as

$$U(\mathbf{R}) = U_0(\mathbf{R}) + 4U_1(\mathbf{R})\frac{\mathbf{t} \cdot \mathbf{T}}{A}, \quad (17)$$

where \mathbf{t} and \mathbf{T} denote the projectile and target isospins, respectively. Proton and neutron optical potentials, U_p and U_n , can be described by the isoscalar and isovector components as

$$U_p = U_0 - \frac{N-Z}{A}U_1, \quad (18)$$

$$U_n = U_0 + \frac{N-Z}{A}U_1, \quad (19)$$

and hence

$$U_0 = \frac{U_p + U_n}{2}, \quad (20)$$

$$U_1 = \frac{U_n - U_p}{2} \frac{A}{N-Z}, \quad (21)$$

where N and Z are the neutron and proton numbers of target nucleus. In the folding model, the difference $U_n - U_p$ is proportional to the difference $\rho_n - \rho_p$ and hence the isovector component U_1 of Eq. (21) is to the factor $(\rho_n - \rho_p)/(N-Z)$ that little depends on $N-Z$. Therefore it follows from Eq. (18) that the contribution of U_1 to U_p linearly increases as $N-Z$ becomes large. In the folding model, the isoscalar part U_0 is proportional to the total density $\rho_n + \rho_p$. Hence the contribution of U_0 to U_p also becomes large as N increases with Z fixed, since so does ρ_n .

Figure 20 shows reaction cross sections for $p+^{20-32}\text{Ne}$ scattering at 65 MeV. The reaction cross sections are calculated with either U_p or U_0 . The closed (open) circles denote the results of U_p (U_0) calculated with the AMD densities. For neutron-rich Ne isotopes $^{24-32}\text{Ne}$, the deviation of the closed circles from the stable-nucleus (dotted) line stems from density-broadening effects due to weak binding, although for $^{20-23}\text{Ne}$ the deviation is originated in density-broadening effects due to deformation. The deviation of the open circles from the stable-nucleus line represents the contribution of U_0 to the density-broadening effects, and the deviation of the closed circles from the open ones does the contribution of U_1 to the density-broadening effects. The contribution of U_1 increases linearly as $N-Z$ becomes large, as expected. Both the contributions are comparable for neutron-rich Ne isotopes $^{24-32}\text{Ne}$.

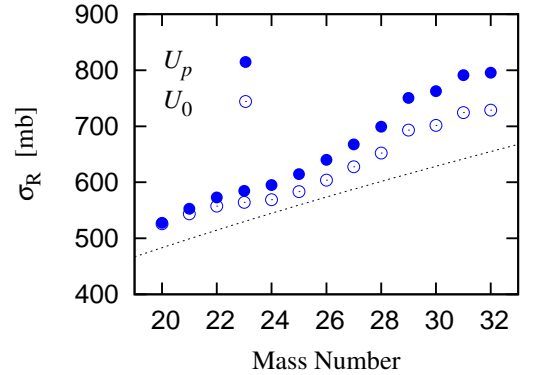


FIG. 20: (Color online) Effects of the isoscalar and isovector components, U_0 and U_1 , on reaction cross sections for proton scattering from $^{20-32}\text{Ne}$ system at 65 MeV. The open (closed) circles denote the results of U_0 (U_p) calculated with the AMD densities. The dotted line means the stable-nucleus line.

Finally, we test the reliability of the isovector component U_1 of the present folding model by analyzing the

charge-exchange (p, n) reaction to isobaric analog states (IAS). The proton- and neutron-channel potentials and the coupling potentials are calculated from the Lane potential Eq. (17); see Ref. [59] for the details of formulation.

Figure 21 shows the differential cross section of $^{22}\text{Ne}(p, n)^{22}\text{F}_{\text{IAS}}$ reaction at 35 MeV. The solid and dotted lines represent the results of the folding model calculated with the AMD and HF densities, respectively. The two lines are close to each other at forward and intermediate angles $\theta_{\text{c.m.}} \lesssim 110^\circ$ where the experimental data [60] are available. The two lines well reproduce the data with no adjustable parameter, indicating that the present model is reliable also for the isovector component. Further analyses will be made in a forthcoming paper.

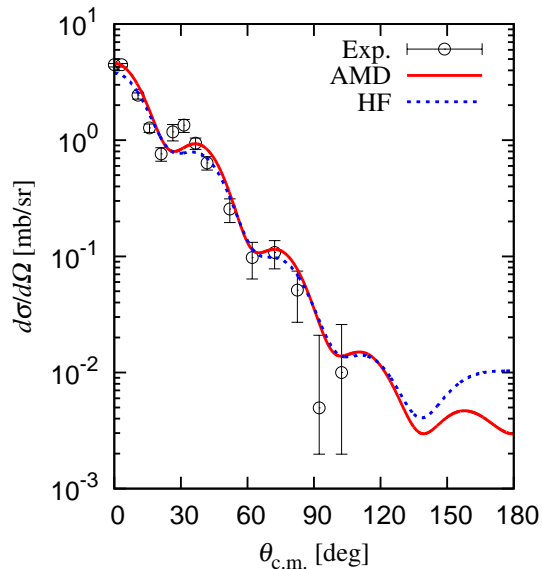


FIG. 21: (Color online) Angular distribution of the differential cross section for $^{22}\text{Ne}(p, n)^{22}\text{F}_{\text{IAS}}$ reaction at 35 MeV. The solid (dotted) line denotes the result of the folding model with the AMD (HF) density. The experimental data are taken from Ref. [60].

IV. SUMMARY

We have derived local microscopic optical potentials systematically for polarized proton scattering at 65 MeV, using the local-potential version of the Melbourne g -matrix folding model that was successful in reproducing nucleus-nucleus scattering [24–26]. The local microscopic optical potentials for proton scattering well reproduce the experimental data on stable target nuclei systematically and have geometries similar to the phenomenological optical potentials such as the Koning-Delaroche [4] and the Dirac phenomenology [5, 6] one. Also for $p+^6\text{He}$ scattering at 71 MeV, the g -matrix folding model yields better

agreement than the t -matrix folding model. Therefore we can say that the local-potential version of the Melbourne g -matrix folding model is a reliable model to describe both nucleon-nucleus and nucleus-nucleus scattering.

The local microscopic optical potentials U are also quite useful in many applications. Furthermore, the local nature makes it easy to clarify global properties of U over both stable and unstable target nuclei. As target nuclei, in this paper we considered ^6He and neutron-rich Ne isotopes in addition to stable nuclei of mass number $A = 4$ –208. In particular, it is interesting to compare properties of U in ^6He and ^{31}Ne with general properties of U in stable nuclei, since ^6He is a typical two-neutron halo nucleus and ^{31}Ne is a one-neutron halo nucleus with large deformation. Throughout the global analyses, we have clarified the A and N dependence of U . The target density is broadened in ^6He by the weak-binding nature and in neutron-rich Ne isotopes by both the weak-binding nature and the nuclear deformation. The density broadening enlarges both the strength and the root-mean-square radius of the central part of U , but for the real spin-orbit part it enlarges the root-mean-square radius but weakens the strength. Density broadening effects due to weak binding and nuclear deformation are conspicuous particularly for halo nuclei such as ^6He and ^{31}Ne . The statement mentioned above is true also for U at intermediate energies such as 200 MeV.

In proton scattering, target deformation not only broadens the spherical part of the folding potential but also enhances target excitations and back reactions to the elastic channel. For neutron-rich unstable target nuclei at 65 MeV, both the effects are appreciable, but density-broadening effects due to weak binding are much more important than the effects. For odd target nuclei with finite total spin, a reorientation of the target spin affects elastic scattering only at middle and backward angles, so the reorientation effects are small on reaction cross sections.

As mentioned above, density-broadening effects are quite important for neutron-rich nuclei. The effects are separated into the isoscalar and isovector components. Both the components yield comparable contributions to the density-broadening effects for neutron-rich nuclei. Finally, we tested the reliability of the isovector component of the present folding model by analyzing the charge-exchange (p, n) reaction to isobaric analog states (IAS). The model well reproduces the experimental data on $^{22}\text{Ne}(p, n)^{22}\text{F}_{\text{IAS}}$ reaction at 35 MeV. The present folding model is thus reliable also for the isovector component. Further analyses will be made for charge-exchange (p, n) reactions in a forthcoming paper.

Acknowledgments

The authors thank T. Furumoto, T. Matsumoto, M. Kohno, K. Ogata, T. Uesaka, and S. Sakaguchi for

useful discussions. This work is supported in part by Grant-in-Aid for Scientific Research (No. 244137) from the Japan Society for the Promotion of Science (JSPS). The numerical calculations of this work were performed on the computing system in Research Institute for Information Technology of Kyushu University.

Appendix A: Definitions of quantities

The explicit forms of $\delta_0^{(\alpha)}(R, s)$ and $\rho_1^{(\alpha)}(R, s)$ are

$$\begin{aligned} \delta_0^{(\alpha)}(R, s) &= \frac{1}{2} \int_{-1}^{+1} d\omega \frac{g_{\text{LS},p\alpha}^{\text{EX}}(s; \rho_\alpha)}{x} \\ &\times \left\{ \frac{3}{k_F^{(\alpha)}(x)s} j_1(k_F^{(\alpha)}(x)s) \frac{d}{dx} \rho_\alpha(x) \right\}_{x=\sqrt{R^2+s^2/4+Rs\omega}} \\ &+ s \rho_\alpha(x) \frac{d}{dx} k_F^{(\alpha)}(x) \Big|_{x=\sqrt{R^2+s^2/4+Rs\omega}} \\ &\times \frac{d}{dy} \left[\frac{3}{y} j_1(y) \right] \Big|_{y=k_F^{(\alpha)}(x)s} \Big\}, \end{aligned} \quad (\text{A1})$$

and

$$\begin{aligned} \rho_1^{(\alpha)}(R, s) &= \frac{1}{2} \int_{-1}^{+1} d\omega \omega g_{\text{LS},p\alpha}^{\text{EX}}(s; \rho_\alpha) \frac{3}{k_F^{(\alpha)}(x)s} \\ &\times j_1(k_F^{(\alpha)}(x)s) \rho_\alpha(y) \Big|_{y=\sqrt{R^2+s^2/4+Rs\omega}}, \end{aligned} \quad (\text{A2})$$

where

$$k_F^{(\alpha)} = (3\pi^2 \rho_\alpha)^{1/3}, \quad (\text{A3})$$

$$g_{\text{LS},pp}^{\text{DR,EX}}(s; \rho_p) = g_{\text{LS}}^{11}, \quad (\text{A4})$$

$$g_{\text{LS},pn}^{\text{DR,EX}}(s; \rho_n) = \frac{1}{2} (\pm g_{\text{LS}}^{10} + g_{\text{LS}}^{11}). \quad (\text{A5})$$

-
- [1] M. Kamimura, M. Yahiro, Y. Iseri, Y. Sakuragi, H. Kameyama, and M. Kawai, *Prog. Theor. Phys. Suppl.* **89**, 1 (1986).
- [2] N. Austern, Y. Iseri, M. Kamimura, M. Kawai, G. Rautscher, and M. Yahiro, *Phys. Rep.* **154**, 125 (1987).
- [3] M. Yahiro, K. Ogata, T. Matsumoto, and K. Minomo, *Prog. Theor. Exp. Phys.* **2012**, 01A206 (2012).
- [4] A. J. Koning and J. P. Delaroche, *Nucl. Phys. A* **713** 231 (2003).
- [5] S. Hama, B. C. Clark, E. D. Cooper, H. S. Sherif, and R. L. Mercer, *Phys. Rev. C* **41**, 2737 (1990).
- [6] E. D. Cooper, S. Hama, B. C. Clark, and R. L. Mercer, *Phys. Rev. C* **47**, 297 (1993).
- [7] C. M. Perey and F. G. Perey, *At. Data Nucl. Data Tables* **17**, 1 (1976).
- [8] T. Uesaka *et al.*, *Phys. Rev. C* **82**, 021602(R) (2010); S. Sakaguchi *et al.*, *Phys. Rev. C* **84**, 024604 (2011).
- [9] K. Kaki, Y. Suzuki, and R. B. Wiringa, *Phys. Rev. C* **86**, 044601 (2012).
- [10] G. Bertsch, J. Borysowicz, H. McManus, and W. G. Love, *Nucl. Phys. A* **284**, 399 (1977).
- [11] J. -P. Jeukenne, A. Lejeune, and C. Mahaux, *Phys. Rev. C* **16**, 80 (1977); J. -P. Jeukenne, A. Lejeune, and C. Mahaux, *Phys. Rep.* **25**, 83 (1976).
- [12] F. A. Brieva and J. R. Rook, *Nucl. Phys. A* **291**, 299 (1977); *ibid.* 291, 317 (1977); *ibid.* 297, 206 (1978).
- [13] G. R. Satchler and W. G. Love, *Phys. Rep.* **55**, 183 (1979).
- [14] G. R. Satchler, "Direct Nuclear Reactions", Oxford University Press, (1983).
- [15] N. Yamaguchi, S. Nagata, and T. Matsuda, *Prog. Theor. Phys.* **70**, 459 (1983); N. Yamaguchi, S. Nagata, and J. Michiyama, *Prog. Theor. Phys.* **76**, 1289 (1986).
- [16] L. Rikus, K. Nakano, and H. V. Von Geramb, *Nucl. Phys. A* **414**, 413 (1984); L. Rikus, and H. V. Von Geramb, *Nucl. Phys. A* **426**, 496 (1984).
- [17] K. Amos, P. J. Dortmans, H. V. Von Geramb, S. Karataglidis, and J. Raynal, in *Advances in Nuclear Physics*, edited by J. W. Negele and E. Vogt (Plenum, New York, 2000) Vol. 25, p. 275.
- [18] T. Furumoto, Y. Sakuragi, and Y. Yamamoto, *Phys. Rev. C* **78**, 044610 (2008); *ibid.*, **79**, 011601(R) (2009); *ibid.*, **80**, 044614 (2009).
- [19] D. T. Khoa, W. von Oertzen, H. G. Bohlen, and S. Ohkubo, *J. Phys. G* **34**, R111 (2007).
- [20] K. Minomo, K. Ogata, M. Kohno, Y. R. Shimizu, and M. Yahiro, *J. Phys. G* **37**, 085011 (2010) [arXiv:0911.1184 [nucl-th]].
- [21] K. M. Watson, *Phys. Rev.* **89**, 575 (1953).
- [22] A. K. Kerman, H. McManus, and R. M. Thaler, *Ann. Phys.* **8**, 551 (1959).
- [23] M. Yahiro, K. Minomo, K. Ogata, and M. Kawai, *Prog. Theor. Phys.* **120**, 767 (2008).
- [24] K. Minomo, T. Sumi, M. Kimura, K. Ogata, Y. R. Shimizu, and M. Yahiro, *Phys. Rev. C* **84**, 034602 (2011).
- [25] K. Minomo, T. Sumi, M. Kimura, K. Ogata, Y. R. Shimizu, and M. Yahiro, *Phys. Rev. Lett.* **108**, 052503 (2012).
- [26] T. Sumi *et al.*, *Phys. Rev. C* **85**, 064613 (2012).
- [27] M. Kimura and H. Horiuchi, *Prog. Theor. Phys.* **111**, 841 (2004).
- [28] M. Kimura, *Phys. Rev. C* **75**, 041302(R) (2007).

- [29] J. F. Berger, M. Girod, and D. Gogny, *Comput. Phys. Commun.* **63**, 365 (1991).
- [30] H. de Vries, C. W. de Jager, and C. de Vries, *At. Data Nucl. Data Tables* **36**, 495 (1987).
- [31] H. F. Arellano, F. A. Brieva, and W. G. Love, *Phys. Rev. C* **52**, 301 (1995).
- [32] R. Machleidt, K. Holinde, and Ch. Elster, *Phys. Rep.* **149**, 1 (1987).
- [33] R. P. Singhal, M. W. S. Macauley, and P. K. A. De Witt Huberts, *Nucl. Instr. and Meth.* **148**, 113 (1978).
- [34] W. G. Love and M. A. Franey, *Phys. Rev. C* **24**, 1073 (1981); M. A. Franey and W. G. Love, *Phys. Rev. C* **31**, 488 (1985).
- [35] K. Imai *et al.*, *Nucl. Phys. A* **325**, 397 (1979).
- [36] K. Fukunaga *et al.*, *Nucl. Phys. A* **456**, 48 (1986).
- [37] S. Kato *et al.*, *Phys. Rev. C* **31**, 1616 (1985).
- [38] M. Ieiri *et al.*, *Nucl. Instr. and Meth. A* **257**, 253 (1987).
- [39] H. Sakaguchi *et al.*, *Phys. Lett. B* **89**, 40 (1979).
- [40] H. Ejiri *et al.*, *Phys. Rev. C* **24**, 2001 (1981).
- [41] T. Noro *et al.*, *Nucl. Phys. A* **366**, 189 (1981).
- [42] H. Sakaguchi *et al.*, *Phys. Lett. B* **99**, 92 (1981).
- [43] A. M. Sourkes, A. Houdayer, W. T. H. van Oers, R. F. Carlson, and R. E. Brown, *Phys. Rev. C* **13**, 451 (1976).
- [44] A. Ingemarsson *et al.*, *Nucl. Phys. A* **653**, 341 (1999).
- [45] R. F. Carlson *et al.*, *Nucl. Phys. A* **445**, 57 (1985).
- [46] N. E. Davison *et al.*, *Nucl. Phys. A* **290**, 45 (1977).
- [47] J. J. H. Menet, E. E. Gross, J. J. Malanify, and A. Zucker, *Phys. Rev. C* **4**, 1114 (1971).
- [48] L. G. Votta, P. G. Roos, N. S. Chant, and R. Woody, III, *Phys. Rev. C* **10**, 520 (1974).
- [49] T. Matsumoto, E. Hiyama, K. Ogata, Y. Iseri, M. Kamimura, S. Chiba, and M. Yahiro, *Phys. Rev. C* **70**, 061601(R) (2004).
- [50] T. Matsumoto, T. Egami, K. Ogata, Y. Iseri, M. Kamimura, and M. Yahiro, *Phys. Rev. C* **73**, 051602(R) (2006).
- [51] G. A. Moss *et al.*, *Phys. Rev. C* **21**, 1932 (1980).
- [52] H. O. Meyer, P. Schwandt, G. L. Moake, and P. P. Singh, *Phys. Rev. C* **23**, 616 (1981).
- [53] H. Seifert *et al.*, *Phys. Rev. C* **47**, 1615 (1993).
- [54] L. Lee *et al.*, *Phys. Lett. B* **205**, 219 (1988).
- [55] A. A. Korshennikov *et al.*, *Nucl. Phys. A* **617**, 45 (1997).
- [56] T. Nakamura *et al.*, *Phys. Rev. Lett.* **103**, 262501 (2009).
- [57] M. Takechi *et al.*, *Phys. Lett. B* **707**, 357 (2012).
- [58] E. Fabrici *et al.*, *Phys. Rev. C* **21**, 844 (1980).
- [59] D. T. Khoa, H. S. Than and D. C. Cuong, *Phys. Rev. C* **76**, 014603 (2007).
- [60] G. C. Jon *et al.*, *Phys. Rev. C* **56**, 900 (1997).